Preprint

Neural Network Based Δ-Machine learning approach efficiently brings the DFT potential energy surface to the CCSD(T) quality: a case for the OH + CH_3OH reaction

Kaisheng Song[1] and Jun Li[1,*]

[1] *School of Chemistry and Chemical Engineering & Chongqing Key Laboratory of Theoretical and Computational Chemistry, Chongqing University, Chongqing 401331, P.R. China*

*: *Corresponding author, email:* jli15@cqu.edu.cn (JL).

Abstract

The recently proposed permutationally invariant polynomial-neural network (PIP-NN) based Δ-machine learning (Δ-ML) approach (PIP-NN Δ-ML, J. Phys. Chem. Lett. 2022, 13, 4729) is a flexible, general, and highly cost-efficient method to develop full dimensional accurate potential energy surface (PES). Only a small portion of points, which can be actively selected from the low-level (often DFT) points, with high-level energies are needed to bring a low-level PES to a high-level of quality. The hydrogen abstraction reaction between methanol and hydroxyl radical, OH + CH_3OH, has been studied by theories and experiments for a long time due to its great importance in combustion, atmospheric and interstellar chemistry. However, it is not trivial to develop the full dimensional accurate PES for it. In this work, the PIP-NN Δ-ML method is successfully applied to the title reaction. The DFT PES was fitted by using 140192 points. Only 5% of the DFT dataset was needed to be calculated at the level of UCCSD(T)-F12a/AVTZ, and to improve the DFT PES to the target high-level, UCCSD(T)-F12a/AVTZ. More than 92% of the original unaffordable calculation cost were saved. The kinetics, including rate coefficients and branching ratios, were then studied by performing quasi-classical trajectory calculations on this newly fitted PES for the title reaction.

1. Introduction

Both hydroxyl radicals (OH) and methanol (CH_3OH) are widely present in many chemistry related scenes, like atmosphere,[1] combustion,[2-4] and interstellar space.[5] Methanol, the simplest alcohol, is a green, clean, renewable and pivotal energy source, which is well recognized not only as a fuel to reduce CO_2 emissions, but also as a source for a variety of complicated organic molecules, such as olefins, carbonyl compounds, peptides and polypeptides, and even RNA.[6] Similar to the F/Cl/H + CH_3OH reactions,[7-10] the reaction between OH and CH_3OH has several product channels. The major channels are the hydrogen abstractions,

$$OH + CH_3OH \rightarrow H_2O + CH_2OH, \quad (R1)$$

$$OH + CH_3OH \rightarrow H_2O + CH_3O. \quad (R2)$$

Over the past decades, the reaction mechanisms and the kinetics of the two channels have been studied comprehensively[1-5, 11-50] by experiment and theory, due to not only their significance in various chemical environments, but also the fundamental role as a prototypical polyatomic reaction with competitive channels.

As shown in **Figure 1**, ample experimental investigations have been carried out to study the rate coefficients (denoted as k, in $cm^3molecule^{-1}s^{-1}$), branching ratios between R1 and R2, as well as kinetic isotope effect. Most experimental measurements focused on kinetics over the temperature between 200 and 2000 K.[2, 13-15, 18-26, 28, 32-36, 49, 51] The measured branching ratios of the R2 channel (defined as k_2 / k_t, $k_t = k_1 + k_2$) were 0.11±0.03,[18] 0.17±0.13,[19] 0.25±0.08,[20] 0.17±0.03,[23] 0.15±0.08[24] at 298 K, 0.22±0.07 at 393 K,[18] and >80% at 900 ~ 1300 K.[34]

Recently, the title reaction was found to play an important role in the interstellar medium. Interestingly, at low temperatures below 200 K, CH_3O becomes the main product due to the quantum tunneling effect and thus an important contributor to the formation of interstellar CH_3O.[5, 52] At 10, 50, and 100 K, the rate coefficients were measured to be 3.0, 0.49, and 0.38×10^{-10} experimentally.[38] Antiñolo et al. obtained the rate coefficients $(3.6\pm0.1) \times 10^{-12}$ $(T/300K)^{-(1.0\pm0.2)}$ over 22 ~ 64 K.[39] Ocana et al. studied the kinetics over 11.7 ~ 177.5 K, and found almost two orders of magnitude increase in the rate coefficient from 175 to 100 K.[48] Gómez Martín studied the kinetics of the title reaction over 56 ~ 202 K,[1] and confirmed that at temperatures below 180 K, the R2 channel dominates due to the quantum tunneling.[5]

Theory is very helpful to provide the dynamic detail along the reaction. The potential feature largely determines the reaction kinetics and dynamics. As shown in **Figure 2**, both R1 and R2 channels have apparent barriers, TS1 and TS2, sharing the same pre-reaction complex, RC, which has been characterized also experimentally.[37] There exist two different product complexes, PC1 and PC2, before arriving at the final products, H_2O + CH_2OH and H_2O + CH_3O. The former product channel is ~10 kcal/mol more exothermic than the latter, and the energy difference between PC1 and PC2 is also similar, ~ 11 kcal/mol. TS1 is ~ 2 kcal/mol lower than TS2. Indeed, the reaction mechanisms of R1 and R2 channels for the title reaction have been studied by various electronic structure levels of theory,[4, 27, 30, 31, 34, 40, 43, 47, 48] such as MP2, MP4, DFT, QCISD(T), G2, CCSD(T), CCSD(T)-F12a and CASPT2, and the kinetics were then determined by statistical rate theories, like transition state theory (TST), Rice-Ramsperger-Kassel-Marcus (RRKM), or master equation. As shown in **Figure 1**, theoretical results are generally consistent with experiment at temperatures above ~300 K. At interstellar low temperatures, kinetics computations based on high-level ab initio information also predicted that the rate coefficients were increased, consistent with experiment, due to quantum tunneling effect. However, the experimental results are still significantly higher than the kinetics calculations. The theoretical studies by Siebrand et al. suggested that methanol dimers can play a significant role in the interstellar low temperature kinetics,[40] which was questioned by the combined experimental and theoretical investigation.[42]

Except the statistical rate theories, dynamic methods, including quasi-classical trajectory (QCT), ring-polymer molecular dynamics, and quantum dynamics (QD), can provide rate coefficients and dynamic details. Roncero et al. developed a full dimensional potential energy surface (denoted as PES-2018) for the reaction OH + CH_3OH, and carried out QCT calculations under 100 K. The results showed the reactivity was increased at low temperature / energy due to the complex forming mechanism. However, the QCT predictions were still lower than the measured ones because the quantum effect was not considered in QCT.[44] The PES-2018 was fitted to more than 2×10^5 points whose energies were calculated at the CCSD(T)-F12a/AVTZ level. The analytical function form included a many-body term that is described by the permutationally invariant polynomial (PIP) method following the method of Aguado et al.[53] and the resulting fitting error was 1.937 kcal/mol.[44]

The performance of the PES is key to determine the dynamic and kinetic properties. The construction of full-dimensional, high fidelity, computationally efficient PESs for chemical systems has been a

challenge for a long time in theoretical and computational chemistry. In the last decade, many machine learning methods for developing PESs have emerged, such as the PIPs,[54] PIP-neural network (PIP-NN),[55-57] and the fundamental invariant-NN (FI-NN).[58] PIP or FI can guarantee the rigorous symmetry property with respect to the permutation of identical atoms, and NN can ensure the high accuracy of the PES. PIP-NN or FI-NN has been successfully employed in fitting full-dimensional accurate PES of many chemical systems[7, 9, 59-67] based on ample points calculated at the UCCSD(T)-F12a/AVTZ level.

It is not trial to develop a full-dimensional accurate PES for the OH + CH_3OH reaction system. One reason is that the title system has 8 atom and 28 degrees of freedom (DOFs), and thus the sampling configuration space is huge, particularly, there exists long-range dipole-dipole interaction in the entrance channel. Another difficulty is the single reference method, UCCSD(T)-F12a, may result in some discontinuity along some dimensions, as the title system is of multi-reference in nature.[68] Although carefully selected Hartee-Fock (HF) orbitals can delete the discontinuity, as proposed by us for the OH + HO_2 system,[61] a single-point energy calculation at the level of UCCSD(T)-F12a/AVTZ[69-71] still takes 30 ~ 70 minutes with 8 cores of a computational node with Intel Xeon CPU E5-2682 v4 @ 2.50GHz. It is expensive to determine the energies of 10^5~10^6 points directly at the UCCSD(T)-F12a/AVTZ level.

Note that the relatively "high-level" PES (V_{HL}) can be improved from a "low-level" PES (V_{LL}). Both the V_{LL} and its difference (ΔV_{HL-LL}) from V_{HL} can be developed efficiently, namely,

$$V_{HL} = V_{LL} + \Delta V_{HL-LL} . \quad (1)$$

Based on this idea, several promising protocols have been proposed, such as the dual-level Shepard interpolation method,[72] the hierarchical construction scheme,[73] the Δ-machine learning (Δ-ML) method.[74-77] As ΔV_{HL-LL}, with a small energy scope, features a very flat characterization, only a much smaller portion of the low-level dataset needs be calculated at the target high-level electronic structure method to fit the correction PES, ΔV_{HL-LL}. In the dual-level Shepard interpolation[72] and the hierarchical construction method,[73] the interpolation was used to represent V_{LL} and ΔV_{HL-LL}, and data points were selected from reduced grids of data points for V_{LL}. In the Δ-ML approach,[75-77] both V_{LL} and ΔV_{HL-LL} were fitted by PIP or fragment-PIP,[78] and the method was successfully applied to developing PESs of several systems, including CH_4, H_3O^+, trans and cis-N-methyl acetamide (NMA), $CH_3CONHCH_3$, and acetylacetone.

The grid approach used in the interpolation for sampling is very expensive for systems with more than 3 atoms. In previous Δ-ML method, the accuracy of the PES fitted by the PIP method cannot be as high as that of the PES fitted by the NN-based method, like PIP-NN or FI-NN. Furthermore, representing V_{HL} of a system as the sum of two PESs, V_{LL} and ΔV_{HL-LL}, would reduce the efficiency of the PES evaluation, particularly in the dynamical calculations.

Very recently, our group proposed a new Δ-ML strategy using PIP-NN for the construction of the full-dimensional high-accuracy PES of complicated systems. Firstly, a suitable low-level method (often DFT) was selected after comprehensively testing and a low-level PES (V_{LL}) is firstly fitted by the PIP-NN method based on ample DFT calculated points that cover all dynamically relevant regions. The next step is to select points from the existing DFT dataset to construct the correction PES (ΔV_{HL-LL}) between V_{LL} and V_{HL}. Then ΔV_{HL-LL} is used to predict the energy differences of the remaining points whose energies are not computed directly at the target high-level method. Namely, the target high-level energy of these remaining points is the sum of the DFT energy and the predicted energy difference by ΔV_{HL-LL}. Finally, all points with the high-level energy are used to fit the target high-level PES. In the new strategy, ΔV_{HL-LL} is used to efficiently determine the energy difference for points that are not computed directly at the high-level method. The final PES is still represented by a single NN function, which is faster than Eq. (1) in evaluation.[67] All NN based PES methods, PIP-NN, FI-NN, or the high-dimensional-NN (HD-NN) proposed by Behler et al.,[79] can be employed.

In order to reduce the cost of constructing the correction PES as much as possible, it is crucial to select points from the DFT dataset. Namely, the selecting should be efficient and the final number of the selected points for high-level calculations need be as few as possible. Note that NN has limited extrapolation ability. That is, for regions lacking sampled points, different NN PESs may give very different predictions.[80] For any DFT point, if several NN correction PESs yield significantly different corrections, then this DFT point should be included to improve the correction PES. This idea, which was used to automatically construct NN PESs without running trajectories,[80, 81] was employed to actively and effectively sample points from the DFT data points. For the HO_2 + HO_2 PES, only 14% points were selected and calculated at the high-level (UCCSD(T)-F12a/AVTZ) to bring the DFT PES to the target UCCSD(T)-F12a level.[67]

In this work, we employ this promising PIP-NN based Δ-ML approach to tackle the construction of

the full-dimensional accurate PES for the title reaction OH + CH_3OH. Briefly, for V_{LL}, 140 192 points are calculated at the level of UM05-2X/6-311+G(3df, 2p),[82] and fitted by the PIP-NN approach. Only 7586 points are calculated at the UCCSD(T)-F12a/AVTZ level, and required to represent the correction PES ΔV_{HL-LL}. Over 92% calculation cost is saved! The fitting error of the final PES is 0.467 kcal/mol. The geometry, energy, harmonic frequency of the stationary points, as well as reaction paths, long-range interactions between fragments are well reproduced, compared to the UCCSD(T)-F12a/AVTZ calculated ones. Then the kinetics of the title reaction, including the rate coefficient and branching ratio, are revisited on this new PES by QCT.

2. Electronic structure calculation

To develop a high-fidelity full-dimensional PES, the first key is to choose a suitable electronic structure method, which should be sufficiently accurate, time-consuming affordably, and provide reliable descriptions for all dynamically relevant regions, including reactants, products, transition states and intermediates, and regions far from the equilibrium of these stationary points.[80, 83] The UCCSD(T)-F12a/AVTZ method has succeeded in developing a series of PESs for reactive and non-reactive systems,[64, 66, 67, 84, 85] and was suggested for effective construction of full-dimensional accurate PESs.[86]

The energies, geometries and harmonic frequencies of the stationary points along R1 and R2 were determined at the level of UCCSD(T)-F12a/AVTZ as implemented in the Molpro program package.[87] The energies and harmonic frequencies are summarized in **Table S1**, and the structural parameters are given in **Figure S1**. The corresponding reaction profile is illustrated in **Figure 2**. Note that all energies are relative the asymptotic reactants, if not specified.

For R1 channel, as shown in **Figure 1**, OH and CH_3OH first form a reaction complex (RC), which is -6.53 kcal/mol in energy relative to the asymptotic reactants. This RC complex is stabilized by the hydrogen bond: the distance between the hydrogen atom of OH and the oxygen atom of CH_3OH is 1.859 Å at the level of UCCSD(T)-F12a/AVTZ. Compared to isolated OH and CH_3OH, the O-H distance of OH is slightly enlarged from 0.971 to 0.978 Å, and the CH_3OH moiety is nearly unchanged. TS1 is 1.39 kcal/mol higher than the asymptotic reactants, and 7.92 kcal/mol above RC. The forming O-H bond and the breaking C-H bond are 1.452 and 1.163 Å, respectively. Via TS1, one H atom of the CH_3 group is abstracted by the attacking reactant OH. Then the newly formed H_2O shifts towards the OH moiety of CH_2OH to yield the PC1 complex, which is stabilized again by the hydrogen bond between the O atom

of H_2O and the H atom of CH_2OH. The PC1 complex, -28.69 kcal/mol lower than the asymptotic reactants, dissociates to the products CH_2OH and H_2O. The reaction energy is -22.10 kcal/mol (-22.7 kcal/mol with ZPE correction), in good agreement with the experimental value of -23.1 ± 0.4 kcal/mol at 0 K.[34]

RC is also involved in the R2 channel. The OH reactant can rotate around OH of the CH_3OH to form TS2, which has a dynamic bond between O of OH and H of OH in CH_3OH. TS2 is 3.86 and 2.47 kcal/mol higher than reactants and TS1, respectively. PC2 is -17.62 kcal/mol, and can directly dissociate to the products CH_3O and H_2O. The product energy of this channel is -12.55 kcal/mol (-13.65 kcal/mol with ZPE correction), in line with the experimental value -13.7 ± 0.8 kcal/mol at 0 K.[34]

For the title reaction of multi-reference nature, particularly in the entrance channel, the single-reference methods, including UCCSD(T)-F12a/AVTZ, may fail to give the correct solutions. The multiconfiguration reference internally contracted configuration interaction (MRCI), the optimal choice, however, is extremely expensive for the title reaction. Besides, CCSD(T) outperforms MRCI for stationary points generally. In the PES construction of the OH + HO_2 system, we found that the wavefunction with the lowest Hartree-Fock (HF) energy from three different initial HF guesses, neutral, anion, and cation species, can make the consequent UCCSD(T)-F12a results smooth and correct.[61] Tests show this method also works well for the title reaction, as shown in **Figure S2**.

3. The PES construction

3.1 The low-level PES, PESL

Similar to our previous strategy for constructing PESs,[57, 62, 88] 140 192 points are sampled to cover all dynamically related regions along the two reaction pathways R1 and R2. These points are calculated at the select low-level method, UM05-2X/6-311+G(3df, 2p),[82] which is implemented in the Gaussian 16 program.[89] Note that unrestricted Hartree-Fock (UHF) computation is used in UM05-2X, while restricted open-shell HF (ROHF) calculation is used in UCCSD(T)-F12a/AVTZ. The choice of the DFT method is not arbitrary and certain requirements need be fulfilled: (1) the DFT method should yield correct and smooth PES curves; (2) the DFT results should be close to the ones calculated by the target level UCCSD(T)-F12a/AVTZ; (3) the DFT calculation should be efficient. As shown in **SI**, UM05-2X/6-311+G(3df, 2p) fulfills these requirements and is the best one among 12 different combinations of DFT and basis sets.

As shown in Figure 3 (a) and (b), these DFT points were sampled in wide configuration space for the R1 and R2 channels. The distances of OH-CH_3OH, H_2O-CH_2OH and H_2O-CH_3O are as long as 12 Å, so that the long-range interactions can be well captured. The insets show the regions around the stationary points are relatively sampled with denser sampling to guarantee the performance around these key regions. The full dimensional DFT PES, named as the low-level PES (PESL), are fitted by PIP-NN to the DFT dataset. The explicit form of the PIP-NN function is as follows,

$$V = b_1^{(3)} + \sum_{k=1}^{K}\left(\omega_{1,k}^{(3)} \cdot f_2\left(b_k^{(2)} + \sum_{j=1}^{J}\left(\omega_{k,j}^{(2)} \cdot f_1\left(b_j^{(1)} + \sum_{i=1}^{I}\omega_{j,i}^{(1)} \cdot G_i\right)\right)\right)\right), \quad (2)$$

In the PIP-NN, all PIPs up to some specified maximum order are used as the input layer of NN. Specifically for the title system, $G_i = \hat{S}\prod_{m<n}^{N} p_{mn}^{l_{mn}}$, i = 1 ~ *I, I =3059*.[56, 90] In the Morse-like variable, $p_{mn} = \exp(-\lambda r_{mn})$, the internuclear distance between the m and n atom is r_{mn} with a universal adjustable constant λ (λ = 1.05 Å^{-1} in this work). $\hat{S}$ is the symmetrization operator of the system that contains all permutation operations among five identical hydrogen atoms, or between two identical oxygen atoms; $\omega_{j,i}^{(l)}$, the weight parameters, connect the ith neuron of (l-1)th layer and the jth neuron of the lth layer; $b_j^{(l)}$ denote the biases parameters of the jth neuron of the lth layer; J and K denote the sizes of neurons of the two hidden layers, respectively; f_1 and f_2, taken as the hyperbolic tangent function, $\tanh(x) = (e^{2x}-1)/(e^{2x}+1)$, are the nonlinear transfer functions for the two hidden layers. The parameters ω and b were determined via the nonlinear least-squares method by minimizing the root mean square error (RMSE),

$$\text{RMSE}=\sqrt{\sum_{i=1}^{N_{\text{data}}}\left(E_{\text{output}}^{i} - E_{\text{target}}^{i}\right)^2 / N_{\text{data}}}. \quad (3)$$

Generally, several different NN architectures, namely with different I, J and K, are tested to obtain better fittings. For each NN architecture, 100~200 NN trainings were carried out with different initial random parameters. For each NN training, the entire dataset was randomly divided into the training (90%),

validation (5%), and test (5%) parts to prevent the "over-fitting" issue. In addition, the fitting was accepted only if all three parts (training, validation, and test) have similar RMSEs, which can efficiently circumvent false extrapolation caused by edge points in the randomly selected validation and test sets. Meanwhile, the maximum deviation was also considered for the choice of PIP-NN PES.

After tests, the DFT PES (denoted as PESL) has the following architecture: the input adopts 3059 PIPs, the first and second hidden layers have 4 and 50 neurons. With a total of 12541 fitting parameters, the final fitting error is 0.470 kcal/mol. The scattered distribution of fitting errors for PESL is shown in Fig. 4(a), which shows that the errors are evenly distributed within the energy range from -28.8 to 120 kcal/mol. The percentages of absolute fitting errors less than 0.2, 0.4 and 0.5 kcal/mol are 50.2%, 74.8% and 81.8%, respectively. The energy distribution of the DFT data points is illustrated in Fig. 4(b), and most points fall in the energy range of 0 ~ 40 kcal/mol.

3.2 The correction PES: $\Delta V_{HL\text{-}LL}$

For $\Delta V_{HL\text{-}LL}$, ~ 1000 points are first selected from the DFT dataset, of which roughly 700 are around the stationary points and 300 are near the minimum energy paths (MEPs). The generalized Euclidean distance criterion is used to screen points that are of similar configurations according to the formula $\chi\{r_i\} = \sqrt{\sum_i^{28} \left|\vec{r_i} - \vec{r_i}'\right|^2}$, where $\left\{\vec{r_i}\right\}$ and $\left\{\vec{r_i}'\right\}$ represent the internuclear distances of the point i and i'.[57] These points are calculated at the UCCSD(T)-F12a/AVTZ level. A preliminary correction PES ($\Delta V_{HL\text{-}LL}$) is fitted to the energy differences of these 1000 points by PIP-NN. Three different NN structures are used to fit $\Delta V_{HL\text{-}LL}$: 3059-4-50-1, 3059-3-100-1, 3059-3-200-1. The corresponding total number of parameters are 12541, 9681, 10181, relatively.

To minimize the random error of the NN fit, four best correction PESs, $\Delta V^i_{HL\text{-}LL}$, i=1~4, with same or different NN architectures were selected to calculate the average energy difference (D) between them. The limited extrapolated properties of the NN function are used to sample points from the DFT dataset, namely,

$$D = \frac{\sum_{i,j}^{4} \left|\Delta V^i_{HL\text{-}LL} - \Delta V^j_{HL\text{-}LL}\right|}{6}. \quad (4)$$

ΔV^i_{HL-LL} and ΔV^j_{HL-LL} denote the ith and jth correction PES, respectively. For a point in the DFT dataset, Eq. (4) is used to guide if this point should be included in the correction PES. A bigger D indicates that

it should be calculated at the UCCSD(T)-F12a/AVTZ level. About 1 000 points are selected at each iteration. The procedure is repeated iteratively until the correction PES is converged. Effectively, the mean absolute total average energy difference (*MTAD*) and the root mean squared difference (*RMSD*) of the correction PES are calculated at each iteration,

$$MTAD = \frac{\sum_{i=1}^{N_{data}} D_i}{N_{data}} \tag{5}$$

$$RMSD = \frac{\sqrt{\sum_{i=1}^{N_{data}} \left(D_i\right)^2}}{N_{data}} \tag{6}$$

where N_{data} and i are the total number of DFT points and the ith point in the DFT dataset. Once both *MTAD* and *RMSD* do not change with additional points, then the correction PES is converged with respect to the number of CCSD(T)-F12 calculated dataset, as shown in **Figure 5**. In the meantime, the MTAD is very close to the RMSD.

Finally, 7586 points, marked as the CC dataset, are selected from the DFT dataset, 140 192 points, and calculated at the level of UCCSD(T)-F12a/AVTZ. These points were used to fit the correction PES, ΔV_{HL-LL}. Figure 3 (c) and (d) display the distribution of the CC dataset along R1 and R2 channels, respectively, with the two reactive bond lengths up to 12 Å. Details near RC, TS1, TS2 and PC2 are given in the inset. Clearly, the CC dataset has a similar distribution to the DFT dataset.

The final correction PES with a total fitting error of 0.180 kcal/mol is the average of four optimal correction PESs, whose fitting errors are 0.194, 0.200, 0.203, 0.207 kcal/mol, respectively. **Figure 6 (a)** demonstrates the scattered distribution of the fitting errors for ΔV_{HL-LL}, with fitting errors less than 0.2 kcal/mol accounting for 84.2%. **Figure 6 (b)** illustrates the histogram of the DFT dataset along the correction energy. Clearly, most points have an absolute energy difference less than 4 kcal/mol, and only a small portion have an absolute energy difference from 4 to 12 kcal/mol. **Figure 6 (c)** depicts the DFT energy versus the difference energy for the DFT dataset.

3.3 The high-level PES: PESH

In our NN based Δ-ML method, the final correction PES ΔV_{HL-LL} is used to bring those DFT points without direct UCCSD(T)-F12a/AVTZ calculation to the UCCSD(T)-F12a/AVTZ quality effectively. The target high-level PES is finally fitted to 140 192 points with high-level energies, 7586 points were

calculated at the level of UCCSD(T)-F12a/AVTZ, and the remaining points, namely, 140192-7586=132606, were predicted as a sum of the DFT energy and its correction. The same NN architecture for PESL is used for fitting PESH and the final fitting error is 0.467 kcal/mol. Note in this work, we focus on the kinetics of the title reaction below 1000 K, and thus the PESH may be not reliable for dynamics and kinetics simulations above 1000 K.

As shown in **Figure 2**, **S1**, and **Table S1**, various properties, including energy, geometry, and harmonic frequency of the stationary points, are well reproduced by PESH, compared to those calculated at the UCCSD(T)-F12a/AVTZ level.

As shown in **Figure 7 (a),** the scattered fitting errors for the correction and entire dataset in the PESH are small in the entire energy range. Figure 7 (b) shows the distribution of the absolute fitting errors for the training and Entire dataset on the PESH. In fact, the absolute fitting errors of the Entire dataset are less than 0.2, 0.4 and 0.5 kcal/mol in 52.3%, 75.9% and 82.4% of the cases respectively. Obviously, there is a slight improvement compared to the PESL.

Figure 8 (a) shows the contour plot of the R1 reaction channel on PESH along the two reactive bonds R_{CH3} and R_{O1H3} with other coordinates fixed at TS1. Similarly, **Figure 8 (b)** depicts the contour plot of the other reaction channel R2 along the two reactive bonds R_{O2H4} and R_{O1H4} with other coordinates fixed at TS2. It can be seen that both contour plots are smooth and the position of the TS1 and TS2.

Figure 9 (a) and (b) show the potentials along the minimum energy path (MEP) from RC to PC1 via TS1 or from RC to PC2 via TS2 on PESH and PESL. Apparently, PESL and PESH are in good agreement with the direct electronic structure calculations, i.e., UM05-2X/6-311+G(3df, 2p) and UCCSD(T)-F12a/AVTZ. Besides, the energy differences along the MEPs are included in the figure. One can see that the correction PES ΔV_{HL-LL} is in line with the energy deviations, F12a-DFT. Both shows that the energy range of the correction PES is small, confirming that the selected DFT method (UM05-2X/6-311+G(3df, 2p)) is suitable.

Further, to demonstrate the performance of the PESH in the asymptotic reactant or product regions, several one-dimensional (1D) scans are shown in **Figure 10**. The PESH is highly in good agreement with the ab initio (UCCSD(T)-F12a/AVTZ) calculation. Overall, the PESH is highly accurate.

4. Kinetics

Kinetics of the title reaction are calculated on the new high-fidelity full-dimensional PESH at

temperatures of 300, 500, 1000 K by the QCT approach implemented in the VENUS96C program package.[91] The rate coefficient is determined according to the following formula:

$$k(T) = q_e \sqrt{\frac{k_B T}{\mu \pi}} \pi b_{\max}^2 \frac{N_r}{N_{total}} \quad (5)$$

where k_B is the Boltzmann constant, and μ for the reduced mass of two reactants. N_r and N_{total} are the number of reactive trajectories and the total number of trajectories. The OH spin-orbit splitting (140 cm^{-1}) was considered in the factor, q_e:[44]

$$q_e = \frac{2}{2 + 2\exp(-201.43/T)} \quad (6)$$

At each temperature of 300, 500, 1000 K, 2~7 x10^5 trajectories were carried out to make sure that the corresponding statistical errors are all less than 5%. All trajectories were launched with the initial separation between two reactants being 10 Å and halted once the distance between two fragments reaches 10.5 Å. The maximum of impact parameter b_{max} was determined by increasing the impact parameter b gradually until no reaction takes place in a small batch of trajectories (often 10^4). Then for each trajectory, the impact parameter b was chosen from a range from 0 to b_{max}, according to the formula $b = b_{max}\zeta^{1/2}$, where ζ is a uniform random number in [0, 1]. The propagations of trajectories were carried out with a time step of 0.05 fs, numerical gradients, and the combined fourth-order Runge–Kutta and sixth-order Adams–Moulton algorithms.[92] Almost all trajectories conserved energy better than 10^{-4} kcal/mol, indicating that PESH is smooth.

The QCT calculated rate coefficients at 300, 500, and 1000 K are 2.36 × 10^{-12}, 4.20 × 10^{-12}, and 1.30 ×10^{-11} $cm^3molecule^{-1}s^{-1}$, respectively. Some available overall rate coefficients are compared in **Figure 11 (a)**. For clarity, only data at 200 ~ 1000 K are included. Many groups measured the rate coefficient at room temperature (282-300 K), and the results, as shown in **Table S3**, were generally consistent with each other, within 0.86 ~ 1.0 × 10^{-12} cm^3 $molecule^{-1}$ s^{-1}. Hess and Tully measured the overall rate coefficients, 5.89 × 10^{-20} × $T^{2.65}$ × exp[444/T] $cm^3molecule^{-1}s^{-1}$ over a temperature range of 294-866 K under a total pressure of 1 atm and k(298 K)=0.943 × 10^{-12} $cm^3molecule^{-1}s^{-1}$.[25] Dillon et al. obtained k (210~351 K) = 6.67× 10^{-18} ×T^2 × exp[140 /T] $cm^3molecule^{-1}s^{-1}$.[33] Atkinson et al.[93] derived k = 6.38 × 10^{-18} × T^2 × exp(144/T) $cm^3molecule^{-1}s^{-1}$ by fitting the overall rate coefficients over the range 210 ~ 866 K

by Wallington et al.,[22] Hess and Tully,[25] Jimenez et al.,[32] and Dillon et al.[33] Liu et al.[49] derived k (210-1344K) = $3.25 \times 10^{-13} \times (T/300)^{2.55} \times \exp[297.8/T]$ $cm^3molecule^{-1}s^{-1}$ by combining their experimental values from 900-1300 K and the high-temperature data from Zaczek et al.[94] with the low temperature data below 1000 K from Hess and Tully,[25] Dillon et al.,[33] and Jimenez et al.[32] One can see that the experiments are consistent with each other.

There are also many theoretical studies on the kinetics of the title reaction. Xu and Lin[34] obtained k (200-3000K) = $4.65 \times 10^{-20} \times T^{2.68} \exp(414/T)$ $cm^3molecule^{-1}s^{-1}$ by the variational transitional state theory, and k (289.18K)=0.70×10^{-12} $cm^3molecule^{-1}s^{-1}$. As mentioned above, Roncero et al.[44] calculated the overall rate coefficients on the PES-2018 by the QCT approach at 10 ~ 400 K and fond that the results increased significantly with the decreasing temperature, which was about a factor of 8 than the low pressure semiclassical results (LPL-CCUS) of Gao et al.,[43] but lower than the experiments due to that the quantum effects at the low temperature. The QCT calculated results are 2.68, 1.91, and 1.38 times the results measured by Liu et al.[49] The rate coefficients calculated by Roncero et al.[44] and Ocana et al.[95] at the high pressure limit (HPL) are higher than other theoretical results, which are close to each other but lower than experiments.

During QCT evolution process and in the final products, the vibrational energy of the system may be lower than the zero point vibrational energy (ZPE). The so called hard-ZPE constraint is applied. Namely, if the vibrational energy of each product is less than its ZPE, then this trajectory is not considered in the final statistics. Further, anharmonicity effects may affect the ZPE. To this end, the scale factor, 0.96. was obtained from the two reactants, OH and CH_3OH, and the corresponding products, CH_2OH, H_2O, and CH_3O, according to the formula,[96] $\lambda = \sum_i^{all}\left(\omega_i^{\text{theory}} \times \tilde{\nu}_i^{\text{expt}}\right) \Big/ \sum_i^{all}\left(\omega_i^{\text{theory}}\right)^2$, where ω_i^{theory} and $\tilde{\nu}_i^{\text{expt}}$ denotes the ith theoretical harmonic frequency (from the results at UCCSD(T)-F12a/AVTZ level in this work) and ith experimental fundamental frequency (in cm^{-1}) (from NIST[97] in this work), respectively. With this modified hard-ZPE constraint, named as hard-aZPE, the QCT results reduce to 0.767×10^{-12}, 1.71×10^{-12}, and 8.00×10^{-12} $cm^3molecule^{-1}s^{-1}$ at 300, 500, and 1000 K, which are in better agreement with available literature data, as shown in **Figure 11 (a)**.

Correspondingly, **Figure 11 (b)** shows the branching ratio of the CH_3O channel. The present QCT results vary from 0.43 to 0.46, and are much higher than the literature data, probably due to various

inherent issues in QCT method. Then, the hard-aZPE results, 0.22, 0.19, 0.26, within 300 ~ 1000 K, demonstrate that the channel of $CH_2OH + H_2O$ always dominates over this temperature range. As shown, the hard-aZPE results are consistent with and slightly higher than the theoretical results of Ocana et al.,[46] Shannon et al.,[5] at 300 ~ 400 K and 425 ~ 900 K, respectively, and the experimental results by Liu et al.[98] at 900 ~ 1000 K. To explore the reaction mechanism, several movies of trajectories are provided in **SI**. The Ring-polymer Molecular dynamics method (RPMD)[99] or other methods, which can well describe the quantum effects, could be used in the future studies of kinetics below 300 K or even at 10 K on this newly fitted PIP-NN PES to explore the temperature dependences of rate coefficients.

5. Conclusions

Conventional ways to develop a full dimensional accurate potential energy surface (PES) based on an enormous number of CCSD(T) calculated points for complicated systems need an unaffordable cost at time and computational resources. In this work, the recently proposed Δ-machine learning (Δ-ML) method based on the permutationally invariant polynomial-neural network (PIP-NN) method, namely, PIP-NN Δ-ML, was successfully applied to develop a highly accurate full-dimensional PES for the complicated reaction system of $OH + CH_3OH$ at the level of UCCSD(T)-F12a/AVTZ. The target high-level (UCCSD(T)) PES is improved from a low-level (DFT method, in this work, UM05-2X/6-311+G(3df, 2p)) PES. Only about 5% (7586) of the DFT dataset (140192) were chosen by utilizing the limited extrapolation capabilities of NN to evaluate and to estimate the uncertainty of the DFT dataset and were used to fit the difference PES between the low- and the high-level methods. Over 92% cost is saved and the final PES is highly accurate, of the UCCSD(T)-F12a/AVTZ accuracy, with a total fitting error of 0.467 kcal/mol.

The prevalent kinetics of the title reaction, including rate coefficients and branching ratio, were calculated on this new PES by the QCT method at 300, 500, and 1000 K. The QCT method cannot consider the quantum effects, such as ZPE, tunneling effect, etc. With the hard-ZPE constraint, the QCT results agree well with the experiments, confirming the high-accuracy of the PES. It is our hope that the PIP-NN Δ-ML method could be a useful tool to pave the way for developing full-dimensional accurate PESs of complicated reaction systems, on which reliable dynamics and kinetics are expected.

Conflicts of interest

There are no conflicts to declare.

Acknowledgments

This work was financially supported by the National Natural Science Foundation of China (contract no. 21973009), the Venture and Innovation Support Program for Chongqing Overseas Returnees (grant no. cx2021071). Ying Zhang and Jia Li are thanked for the preceding calculations on the title reaction. Dr. Yang Liu is also acknowledged for helpful discussions and assistances, particularly for the PIP-NN based Δ-ML method.

References

1. Gómez Martín, J. C.; Caravan, R. L.; Blitz, M. A.; Heard, D. E.; Plane, J. M. C., Low Temperature Kinetics of the CH3OH + OH Reaction. *J. Phys. Chem. A* **2014,** *118* (15), 2693-2701.

2. Bowman, C. T., A shock-tube investigation of the high-temperature oxidation of methanol. *Combust. Flame* **1975,** *25*, 343-354.

3. Westbrook, C. K.; Dryer, F. L., Comprehensive Mechanism for Methanol Oxidation. *Combust. Sci. Technol.* **1979,** *20* (3-4), 125-140.

4. Galano, A.; Alvarez-Idaboy, J. R.; Bravo-Perez, G.; Ruiz-Santoyo, M. E., Gas phase reactions of C-1-C-4 alcohols with the OH radical: A quantum mechanical approach. *Phys. Chem. Chem. Phys.* **2002,** *4* (19), 4648-4662.

5. Shannon, R. J.; Blitz, M. A.; Goddard, A.; Heard, D. E., Accelerated chemistry in the reaction between the hydroxyl radical and methanol at interstellar temperatures facilitated by tunnelling. *Nat. Chem.* **2013,** *5* (9), 745-749.

6. Mathew, T.; Esteves, P. M.; Prakash, G. K. S., Methanol in the RNA world: An astrochemical perspective. *Front. Astron. Space Sci.* **2022,** *9*.

7. Weichman, M. L.; DeVine, J. A.; Babin, M. C.; Li, J.; Guo, L.; Ma, J.; Guo, H.; Neumark, D. M., Feshbach resonances in the exit channel of the F + CH_3OH --> HF + CH_3O reaction observed using transition-state spectroscopy. *Nat Chem* **2017,** *9* (10), 950-955.

8. Lu, D.; Li, J.; Guo, H., Comprehensive Investigations of the Cl + CH_3OH → HCl + CH_3O/CH_2OH Reaction: Validation of Experiment and Dynamic Insights. *CCS Chem.* **2020,** *2*, 882–894.

9. Lu, D.; Behler, J.; Li, J., Accurate Global Potential Energy Surfaces for the H + CH_3OH Reaction by Neural Network Fitting with Permutation Invariance. *J. Phys. Chem. A* **2020,** *124*, 5737-5745.

10. Tao, C.; Li, J., Ab initio characterization of the potential energy profiles for the multi-channel reactions: H/Cl + CH3OH. *Computational and Theoretical Chemistry* **2022,** *1217*, 113906.

11. Osif, T. L.; Simonaitis, R.; Heicklen, J., The reactions of O(1D) and HO with CH3OH. *Journal of Photochemistry* **1975,** *4* (4), 233-240.

12. Campbell, I. M.; McLaughlin, D. F.; Handy, B. J., RATE CONSTANTS FOR REACTIONS OF HYDROXYL RADICALS WITH ALCOHOL VAPORS AT 292 K. *Chem. Phys. Lett.* **1976,** *38* (2), 362-364.

13. Overend, R.; Paraskevopoulos, G., RATES OF OH RADICAL REACTIONS .4. REACTIONS WITH METHANOL,

ETHANOL, 1-PROPANOL, AND 2-PROPANOL AT 296-K. *J. Phys. Chem.* **1978,** *82* (12), 1329-1333.

14. Ravishankara, A. R.; Davis, D. D., Kinetic rate constants for the reaction of hydroxyl with methanol, ethanol, and tetrahydrofuran at 298 K. *J. Phys. Chem.* **1978,** *82* (26), 2852-2853.

15. Vandooren, J.; Van Tiggelen, P. J., Experimental investigation of methanol oxidation in flames: Mechanisms and rate constants of elementary steps. *Symposium (International) on Combustion* **1981,** *18* (1), 473-483.

16. Tsuboi, T.; Hashimoto, K., Shock tube study on homogeneous thermal oxidation of methanol ☆. *Combustion & Flame* **1981,** *42* (81), 61-76.

17. Barnes, I.; Bastian, V.; Becker, K. H.; Fink, E. H.; Zabel, F., Reactivity studies of organic substances towards hydroxyl radicals under atmospheric conditions. *Atmospheric Environment* **1982,** *16* (3), 545-550.

18. Haegele, J.; Lorenz, K.; Rhaesa, D.; Zellner, R., Rate constants and methoxy (CH3O) product yield of the reaction hydroxyl + methanol -> products. *Ber. Bunsenges. Phys. Chem.* **1983,** *87*, 1023-1026.

19. Meier, U.; Grotheer, H. H.; Just, T., Temperature dependence and branching ratio of the CH 3 OH + OH reaction. *Chem. Phys. Lett.* **1984,** *106* (1–2), 97-101.

20. Meier, U.; Grotheer, H. H.; Riekert, G.; Just, T., Study of Hydroxyl Reactions with Methanol and Ethanol by Laser-induced Fluorescence. *Ber. Bunsenges. Phys. Chem.* **1985,** *89* (3), 325-327.

21. Greenhill, P. G.; Ogrady, B. V., THE RATE-CONSTANT OF THE REACTION OF HYDROXYL RADICALS WITH METHANOL, ETHANOL AND (D3)METHANOL. *Australian Journal of Chemistry* **1986,** *39* (11), 1775-1787.

22. Wallington, T. J.; Kurylo, M. J., THE GAS-PHASE REACTIONS OF HYDROXYL RADICALS WITH A SERIES OF ALIPHATIC-ALCOHOLS OVER THE TEMPERATURE-RANGE 240-440-K. *Int. J. Chem. Kinet.* **1987,** *19* (11), 1015-1023.

23. Pagsberg, P.; Munk, J.; Sillesen, A.; Anastasi, C., UV SPECTRUM AND KINETICS OF HYDROXYMETHYL RADICALS. *Chem. Phys. Lett.* **1988,** *146* (5), 375-381.

24. McCaulley, J. A.; Kelly, N.; Golde, M. F.; Kaufman, F., Kinetic studies of the reactions of F and OH with CH_3OH. *J. Phys. Chem.* **1989,** *93* (3), 1014-1018.

25. Hess, W. P.; Tully, F. P., Hydrogen-atom abstraction from methanol by hydroxyl radical. *J. Phys. Chem.* **1989,** *93* (5), 1944-1947.

26. Bott, J. F.; Cohen, N., A SHOCK-TUBE STUDY OF THE REACTIONS OF THE HYDROXYL RADICAL WITH SEVERAL COMBUSTION SPECIES. *Int. J. Chem. Kinet.* **1991,** *23* (12), 1075-1094.

27. Pardo, L.; Banfelder, J. R.; Osman, R., THEORETICAL-STUDIES OF THE KINETICS, THERMOCHEMISTRY, AND MECHANISM OF H-ABSTRACTION FROM METHANOL AND ETHANOL. *J. Am. Chem. Soc.* **1992,** *114* (7), 2382-2390.

28. Dóbé, S.; Bérces, T.; Temps, F.; Wagner, H. G.; Ziemer, H., Formation of methoxy and hydroxymethyl free radicals in selected elementary reactions. *Symposium (International) on Combustion* **1994,** *25* (1), 775-781.

29. Li, S. C.; Williams, F. A., Experimental and numerical studies of two-stage methanol flames. *Symp. (Int.) Combust.* **1996,** *26* (1), 1017-1024.

30. Jodkowski, J. T.; Rayez, M. T.; Rayez, J. C.; Berces, T.; Dobe, S., Theoretical study of the kinetics of the hydrogen abstraction from methanol. 3. Reaction of methanol with hydrogen atom, methyl, and hydroxyl radicals. *J. Phys. Chem. A* **1999,** *103* (19), 3750-3765.

31. Bottoni, A.; Casa, P. D.; Poggi, G., Reactions between the OH radical and oxygen-containing atmospheric pollutants: a theoretical description. *Journal of Molecular Structure: THEOCHEM* **2001,** *542* (1), 123-137.

32. Jimenez, E.; Gilles, M. K.; Ravishankara, A. R., Kinetics of the reactions of the hydroxyl radical with CH3OH and C2H5OH between 235 and 360 K. *Journal of Photochemistry and Photobiology a-Chemistry* **2003,** *157* (2-3), 237-245.

33. Dillon, T. J.; Holscher, D.; Sivakumaran, V.; Horowitz, A.; Crowley, J. N., Kinetics of the reactions of HO with methanol (210-351 K) and with ethanol (216-368 K). *Phys. Chem. Chem. Phys.* **2005,** *7* (2), 349-355.

34. Xu, S.; Lin, M. C., Theoretical study on the kinetics for OH reactions with CH3OH and C2H5OH. *Proceed. Combust. Inst.* **2007,** *31*, 159-166.
35. Srinivasan, N. K.; M.C. Su, a.; Michael, J. V., High-Temperature Rate Constants for CH3OH + Kr → Products, OH + CH3OH → Products, OH + (CH3)2CO → CH2COCH3 + H2O, and OH + CH3 → CH2 + H2O†. *J. Phys. Chem. A* **2007,** *111* (19), 3951-3958.
36. Feilberg, K. L.; Gruber-Stadler, M.; Johnson, M. S.; Mühlhäuser, M.; Nielsen, C. J., 13C, 18O, and D Fractionation Effects in the Reactions of CH3OH Isotopologues with Cl and OH Radicals. *J. Phys. Chem. A* **2008,** *112* (44), 11099-11114.
37. Hernandez, F. J.; Brice, J. T.; Leavitt, C. M.; Pino, G. A.; Douberly, G. E., Infrared Spectroscopy of OH··CH3OH: Hydrogen-Bonded Intermediate Along the Hydrogen Abstraction Reaction Path. *J. Phys. Chem. A* **2015,** *119* (29), 8125-8132.
38. Acharyya, K.; Herbst, E.; Caravan, R. L.; Shannon, R. J.; Blitz, M. A.; Heard, D. E., The importance of OH radical–neutral low temperature tunnelling reactions in interstellar clouds using a new model. *Molecular Physics* **2015,** *113* (15-16), 2243-2254.
39. Antinolo, M.; Agundez, M.; Jimenez, E.; Ballesteros, B.; Canosa, A.; El Dib, G.; Albaladejo, J.; Cernicharo, J., REACTIVITY OF OH AND CH3OH BETWEEN 22 AND 64 K: MODELING THE GAS PHASE PRODUCTION OF CH3O IN BARNARD 1b. *Astrophysical J.* **2016,** *823* (1).
40. Siebrand, W.; Smedarchina, Z.; Martínez-Núñez, E.; Fernández-Ramos, A., Methanol dimer formation drastically enhances hydrogen abstraction from methanol by OH at low temperature. *Phys. Chem. Chem. Phys.* **2016,** *18* (32), 22712.
41. Jara-Toro, R. A.; Hernández, F. J.; Taccone, R. A.; Lane, S. I.; Pino, G. A., Water Catalysis of the Reaction between Methanol and OH at 294 K and the Atmospheric Implications. *Angewandte Chemie International Edition* **2017,** *56* (8), 2166-2170.
42. Shannon, R. J.; Martin, J. C. G.; Caravan, R. L.; Blitz, M. A.; Plane, J. M. C.; Heard, D. E.; Antinolo, M.; Agundez, M.; Jimenez, E.; Ballesteros, B.; Canosa, A.; El Dib, G.; Albaladejo, J.; Cernicharo, J., Comment on "Methanol dimer formation drastically enhances hydrogen abstraction from methanol by OH at low temperature". *Phys. Chem. Chem. Phys.* **2018,** *20* (12), 8349-8354.
43. Gao, L. G.; Zheng, J.; Fernández-Ramos, A.; Truhlar, D. G.; Xu, X., Kinetics of the Methanol Reaction with OH at Interstellar, Atmospheric, and Combustion Temperatures. *J. Am. Chem. Soc.* **2018,** *140* (8), 2906-2918.
44. Roncero, O.; Zanchet, A.; Aguado, A., Low temperature reaction dynamics for CH3OH + OH collisions on a new full dimensional potential energy surface. *Phys. Chem. Chem. Phys.* **2018,** *20* (40), 25951-25958.
45. Canosa, A., Gas phase reaction kinetics of complex organic molecules at temperatures of the interstellar medium: The OH + CH3OH case. *Proceedings of the International Astronomical Union* **2019,** *15* (S350), 35-40.
46. Ocaña, A. J.; Blázquez, S.; González, D.; Potapov, A.; Ballesteros, B.; Canosa, A.; Antiñolo, M.; Albaladejo, J.; Jiménez, E., Gas-phase reactivity of CH3OH+OH down to 11.7 K: Astrophysical implications. *Proceedings of the International Astronomical Union* **2019,** *15* (S350), 365-367.
47. Nguyen, T. L.; Ruscic, B.; Stanton, J. F., A master equation simulation for the (OH)-O-center dot + CH3OH reaction. *J. Chem. Phys.* **2019,** *150* (8).
48. Ocana, A. J.; Blazquez, S.; Potapov, A.; Ballesteros, B.; Canosa, A.; Antinolo, M.; Vereecken, L.; Albaladejo, J.; Jimenez, E., Gas-phase reactivity of CH_3OH toward OH at interstellar temperatures (11.7-177.5 K): experimental and theoretical study. *Phys. Chem. Chem. Phys.* **2019,** *21* (13), 6942-6957.
49. Liu, D. P.; Giri, B. R.; Farooq, A., A shock tube kinetic study on the branching ratio of methanol plus OH reaction. *Proceed. Combust. Inst.* **2019,** *37* (1), 153-162.

50. Ali, M. A.; Balaganesh, M.; Al-Odail, F. A.; Lin, K. C., Effect of ammonia and water molecule on OH+CH_3OH reaction under tropospheric condition. *Scientific Reports* **2021,** *11* (1), 12185.
51. Picquet, B. n. d.; Heroux, S. b.; Chebbi, A.; Doussin, J.-F.; Durand-Jolibois, R. g.; Monod, A.; Loirat, H. l. n.; Carlier, P., Kinetics of the Reactions of OH Radicals with some Oxygenated Volatile Organic Compounds under Simulated Atmospheric Conditions. *Int. J. Chem. Kinet.* **1998,** *30*, 839.
52. Cernicharo, J.; Marcelino, N.; Roueff, E.; Gerin, M.; Jiménezescobar, A.; Muñoz Caro, G. M., Discovery of the Methoxy Radical, CH3O, toward B1: Dust Grain and Gas-phase Chemistry in Cold Dark Clouds. *Astrophysical Journal Letters* **2012,** *759* (2), 1445-1449.
53. Aguado, A.; Suarez, C.; Paniagua, M., Accurate global fit of the H_4 potential energy surface. *J. Chem. Phys.* **1994,** *101*, 4004.
54. Qu, C.; Yu, Q.; Bowman, J. M., Permutationally Invariant Potential Energy Surfaces. *Annu. Rev. Phys. Chem.* **2018,** *69* (1), 151-175.
55. Jiang, B.; Guo, H., Permutation invariant polynomial neural network approach to fitting potential energy surfaces. *J. Chem. Phys.* **2013,** *139*, 054112.
56. Li, J.; Jiang, B.; Guo, H., Permutation invariant polynomial neural network approach to fitting potential energy surfaces. II. Four-atom systems. *J. Chem. Phys.* **2013,** *139*, 204103.
57. Jiang, B.; Li, J.; Guo, H., Potential Energy Surfaces from High Fidelity Fitting of Ab Initio Points: The Permutation Invariant Polynomial Neural Network Approach. *Int. Rev. Phys. Chem.* **2016,** *35*, 479.
58. Shao, K.; Chen, J.; Zhao, Z.; Zhang, D. H., Communication: Fitting potential energy surfaces with fundamental invariant neural network. *J. Chem. Phys.* **2016,** *145* (7), 071101.
59. Li, J.; Guo, H., Communication: An accurate full 15 dimensional permutationally invariant potential energy surface for the OH + CH_4 → H_2O + CH_3 reaction. *J. Chem. Phys.* **2015,** *143* (22), 221103.
60. Fu, B.; Zhang, D. H., Ab Initio Potential Energy Surfaces and Quantum Dynamics for Polyatomic Bimolecular Reactions. *J. Chem. Theory Comput.* **2018,** *14* (5), 2289-2303.
61. Liu, Y.; Bai, M.; Song, H.; Xie, D.; Li, J., Anomalous kinetics of the reaction between OH and HO_2 on an accurate triplet state potential energy surface. *Phys. Chem. Chem. Phys.* **2019,** *21* (23), 12667-12675.
62. Jiang, B.; Li, J.; Guo, H., High-Fidelity Potential Energy Surfaces for Gas-Phase and Gas–Surface Scattering Processes from Machine Learning. *J. Phys. Chem. Lett.* **2020,** *11* (13), 5120-5131.
63. Liu, Y.; Li, J., Quantitative Dynamics of the N_2O + C_2H_2 → Oxadiazole Reaction: A Model for 1,3-Dipolar Cycloadditions. *ACS Omega* **2020,** *5* (36), 23343-23350.
64. Xu, X. H.; Li, J., Deciphering Dynamics of the Cl + SiH_4 -> H + SiH_3Cl Reaction on a Machine Learning Made Globally Accurate Full-Dimensional Potential Energy Surface. *J. Phys. Chem. A* **2022,** *126* (37), 6456.
65. Song, K.; Song, H.; Li, J., Validating experiments for the reaction H_2 + NH_2^- by dynamical calculations on an accurate full-dimensional potential energy surface. *Phys. Chem. Chem. Phys.* **2022,** *24* (17), 10160-10167.
66. Qin, J.; Liu, Y.; Li, J., Quantitative dynamics of paradigmatic S_N2 reaction OH^- + CH_3F on accurate full-dimensional potential energy surface. *J. Chem. Phys.* **2022,** *157* (12), 124301.
67. Liu, Y.; Li, J., Permutation-Invariant-Polynomial Neural-Network-Based Δ-Machine Learning Approach: A Case for the HO2 Self-Reaction and Its Dynamics Study. *J. Phys. Chem. Lett.* **2022,** *13* (21), 4729-4738.
68. Győri, T.; Czakó, G., ManyHF: A pragmatic automated method of finding lower-energy Hartree–Fock solutions for potential energy surface development. *J. Chem. Phys.* **2022,** *156* (7), 071101.
69. Adler, T. B.; Knizia, G.; Werner, H.-J., A simple and efficient CCSD(T)-F12 approximation. *J. Chem. Phys.* **2007,**

127, 221106.
70. Knizia, G.; Adler, T. B.; Werner, H.-J., Simplified CCSD(T)-F12 methods: Theory and benchmarks. *J. Chem. Phys.* **2009,** *130*, 054104.
71. Kong, L.; Bischoff, F. A.; Valeev, E. F., Explicitly correlated R12/F12 methods for electronic structure. *Chem. Rev.* **2011,** *112* (1), 75-107.
72. Nguyen, K. A.; Rossi, I.; Truhlar, D. G., A dual-level Shepard interpolation method for generating potential energy surfaces for dynamics calculations. **1995,** *103* (13), 5522-5530.
73. Fu, B.; Xu, X.; Zhang, D. H., A hierarchical construction scheme for accurate potential energy surface generation: An application to the F+H_2 reaction. *J. Chem. Phys.* **2008,** *129* (1), 011103.
74. Ramakrishnan, R.; Dral, P. O.; Rupp, M.; von Lilienfeld, O. A., Big Data Meets Quantum Chemistry Approximations: The Delta-Machine Learning Approach. *J. Chem. Theory Comput.* **2015,** *11* (5), 2087-2096.
75. Zaspel, P.; Huang, B.; Harbrecht, H.; von Lilienfeld, O. A., Boosting Quantum Machine Learning Models with a Multilevel Combination Technique: Pople Diagrams Revisited. *J. Chem. Theory Comput.* **2019,** *15* (3), 1546-1559.
76. Nandi, A.; Qu, C.; Houston, P. L.; Conte, R.; Bowman, J. M., Delta-machine learning for potential energy surfaces: A PIP approach to bring a DFT-based PES to CCSD(T) level of theory. *J. Chem. Phys.* **2021,** *154* (5), 051102.
77. Qu, C.; Houston, P. L.; Conte, R.; Nandi, A.; Bowman, J. M., Breaking the Coupled Cluster Barrier for Machine-Learned Potentials of Large Molecules: The Case of 15-Atom Acetylacetone. *J. Phys. Chem. Lett.* **2021,** *12* (20), 4902-4909.
78. Qu, C.; Bowman, J. M., A fragmented, permutationally invariant polynomial approach for potential energy surfaces of large molecules: Application to N-methyl acetamide. *J. Chem. Phys.* **2019,** *150* (14), 141101.
79. Behler, J.; Parrinello, M., Generalized neural-network representation of high-dimensional potential-energy surfaces. *Phys. Rev. Lett.* **2007,** *98*, 146401.
80. Behler, J., Neural network potential-energy surfaces in chemistry: a tool for large-scale simulations. *Phys. Chem. Chem. Phys.* **2011,** *13* (40), 17930-17955.
81. Lin, Q.; Zhang, Y.; Zhao, B.; Jiang, B., Automatically growing global reactive neural network potential energy surfaces: A trajectory-free active learning strategy. *J. Chem. Phys.* **2020,** *152* (15), 154104.
82. Zhao, Y.; Schultz, N. E.; Truhlar, D. G., Design of Density Functionals by Combining the Method of Constraint Satisfaction with Parametrization for Thermochemistry, Thermochemical Kinetics, and Noncovalent Interactions. *J. Chem. Theory Comput.* **2006,** *2* (2), 364-382.
83. Li, J.; Liu, Y., Data Quality, Data Sampling and Data Fitting: A Tutorial Guide for Constructing Full-dimensional Accurate Potential Energy Surfaces (PESs) of Small Molecular Systems. . In *ChemRxiv. Cambridge: Cambridge Open Engage; 2022; This content is a preprint and has not been peer-reviewed.*, Chen Qu, H. L., Ed. Springer Nature: 2022.
84. Liu, Y.; Li, J.; Felker, P. M.; Bačić, Z., HCl–H_2O dimer: an accurate full-dimensional potential energy surface and fully coupled quantum calculations of intra- and intermolecular vibrational states and frequency shifts. *Phys. Chem. Chem. Phys.* **2021,** *23* (12), 7101-7114.
85. Lu, D.; Chen, J.; Guo, H.; Li, J., Vibrational energy pooling via collisions between asymmetric stretching excited CO_2: a quasi-classical trajectory study on an accurate full-dimensional potential energy surface. *Phys. Chem. Chem. Phys.* **2021,** *23* (42), 24165-24174.
86. Czakó, G.; Szabó, I.; Telekes, H., On the choice of the ab initio level of theory for potential energy surface developments. *J. Phys. Chem. A* **2014,** *118*, 646–654.
87. Werner, H.-J.; Knowles, P. J.; Manby, F. R.; Black, J. A.; Doll, K.; Heßelmann, A.; Kats, D.; Köhn, A.; Korona, T.; Kreplin, D. A.; Ma, Q.; MillerIII, T. F.; Mitrushchenkov, A.; Peterson, K. A.; Polyak, I.; Rauhut, G.; Sibaev, M., The Molpro quantum chemistry package. *J. Chem. Phys.* **2020,** *152* (14), 144107.

88. Li, J.; Zhao, B.; Xie, D.; Guo, H., Advances and New Challenges to Bimolecular Reaction Dynamics Theory. *J. Phys. Chem. Lett.* **2020,** *11* (20), 8844-8860.
89. M. J. Frisch, G. W. T., H. B. Schlegel, G. E. Scuseria, M. A. Robb, J. R. Cheeseman, G. Scalmani, V. Barone, G. A. Petersson, H. Nakatsuji, X. Li, M. Caricato, A. V. Marenich, J. Bloino, B. G. Janesko, R. Gomperts, B. Mennucci, H. P. Hratchian, J. V. Ortiz, A. F. Izmaylov, J. L. Sonnenberg, D. Williams-Young, F. Ding, F. Lipparini, F. Egidi, J. Goings, B. Peng, A. Petrone, T. Henderson, D. Ranasinghe, V. G. Zakrzewski, J. Gao, N. Rega, G. Zheng, W. Liang, M. Hada, M. Ehara, K. Toyota, R. Fukuda, J. Hasegawa, M. Ishida, T. Nakajima, Y. Honda, O. Kitao, H. Nakai, T. Vreven, K. Throssell, J. A. Montgomery, Jr., J. E. Peralta, F. Ogliaro, M. J. Bearpark, J. J. Heyd, E. N. Brothers, K. N. Kudin, V. N. Staroverov, T. A. Keith, R. Kobayashi, J. Normand, K. Raghavachari, A. P. Rendell, J. C. Burant, S. S. Iyengar, J. Tomasi, M. Cossi, J. M. Millam, M. Klene, C. Adamo, R. Cammi, J. W. Ochterski, R. L. Martin, K. Morokuma, O. Farkas, J. B. Foresman, and D. J. Fox, Gaussian, Inc., Wallingford CT, 2016. Gaussian 16, Revision A.03., **2016**.
90. Lu, D.; Li, J., Full-dimensional global potential energy surfaces describing abstraction and exchange for the H + H_2S reaction. *J. Chem. Phys.* **2016,** *145* (1), 014303.
91. Hase, W. L.; Duchovic, R. J.; Hu, X.; Komornicki, A.; Lim, K. F.; Lu, D.-H.; Peslherbe, G. H.; Swamy, K. N.; Linde, S. R. V.; Varandas, A.; Wang, H.; Wolf, R. J., VENUS96: A General Chemical Dynamics Computer Program. *Quantum Chemistry Program Exchange Bulletin* **1996,** *16*, 671.
92. Bunker, D. L., Classical trajectory methods. *Meth. Comp. Phys.* **1971,** *10*, 287-325.
93. Atkinson, R.; Baulch, D. L.; Cox, R. A.; Crowley, J. N.; Hampson, R. F.; Hynes, R. G.; Jenkin, M. E.; Rossi, M. J.; Troe, J., Evaluated kinetic and photochemical data for atmospheric chemistry: Volume II; gas phase reactions of organic species. *Atmos. Chem. Phys.* **2006,** *6* (11), 3625-4055.
94. Zaczek, L. T.; Lam, K. Y.; Davidson, D. F.; Hanson, R. K., A shock tube study of CH3OH+OH⟶Products using OH laser absorption. *Proceed. Combust. Inst.* **2015,** *35* (1), 377-384.
95. Ocaña, A. J.; Blázquez, S.; Potapov, A.; Ballesteros, B.; Canosa, A.; Antiñolo, M.; Vereecken, L.; Albaladejo, J.; Jiménez, E., Gas-phase reactivity of CH3OH toward OH at interstellar temperatures (11.7–177.5 K): experimental and theoretical study. *Phys. Chem. Chem. Phys.* **2019,** *21* (13), 6942-6957.
96. Merrick, J. P.; Moran, D.; Radom, L., An Evaluation of Harmonic Vibrational Frequency Scale Factors. *J. Phys. Chem. A* **2007,** *111* (45), 11683-11700.
97. NIST Computational Chemistry Comparison and Benchmark Database
NIST Standard Reference Database Number 101
Release 22, May 2022. http://cccbdb.nist.gov/.
98. Liu, D.; Giri, B. R.; Farooq, A., A shock tube kinetic study on the branching ratio of methanol + OH reaction. *Proceed. Combust. Inst.* **2019,** *37* (1), 153-162.
99. Suleimanov, Y. V.; Aoiz, F. J.; Guo, H., Chemical Reaction Rate Coefficients from Ring Polymer Molecular Dynamics: Theory and Practical Applications. *J. Phys. Chem. A* **2016,** *120* (43), 8488-8502.

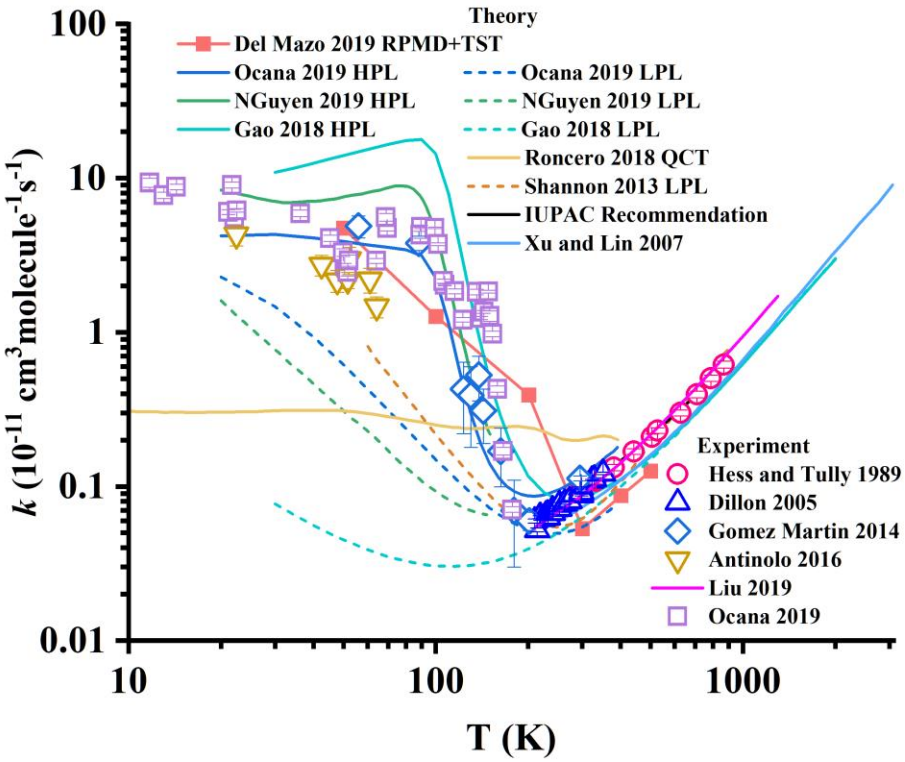

Figure 1. Overall rate coefficients of the OH + CH_3OH reaction at the temperature from 10 to 1200 K.

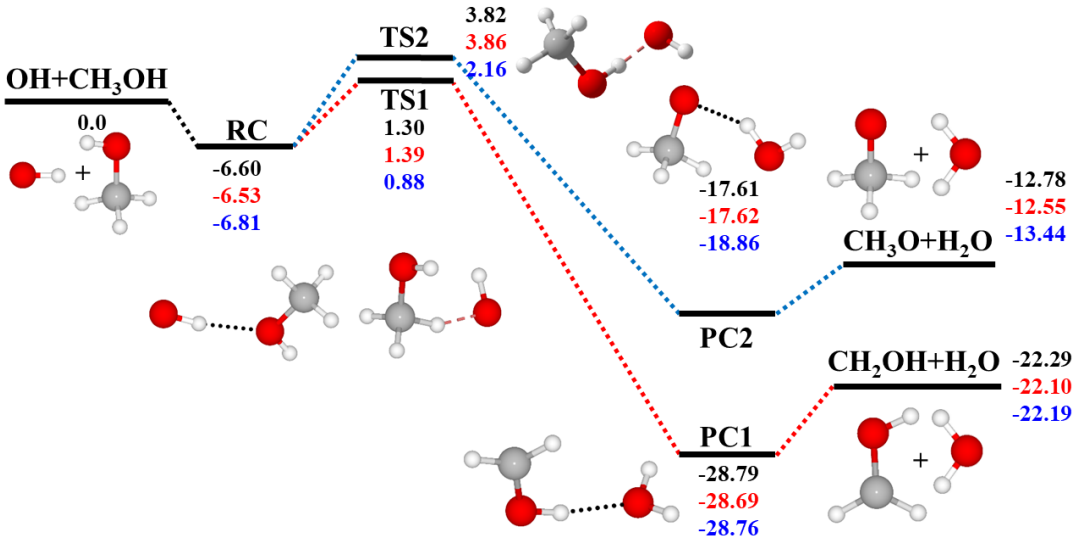

Figure 2. Schematic reaction profile for the OH + CH_3OH → CH_2OH / CH_3O + H_2O reaction. Energies are in kcal mol^{-1} and relative to the reactant asymptote: PESH, UCCSD(T)-F12a/AVTZ, M05-2X/6-311+G(3df, 2p).

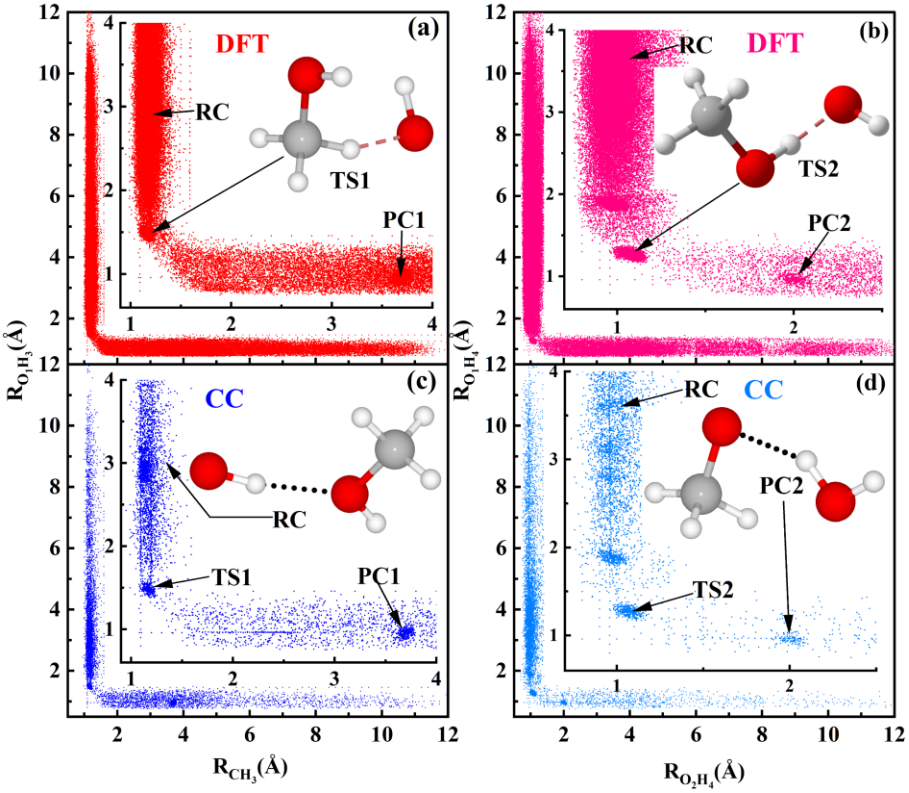

Figure 3. (a)/(b) Distribution of the DFT dataset for V_{LL} along the two reactive bond length up to 12 Å. The inset plots show the details near the transition state. (c)/(d) Similar to (a)/(b) but for the UCCSD(T)-F12a/AVTZ calculated dataset. (a) and (c) for R1, and (b) and (d) for R2.

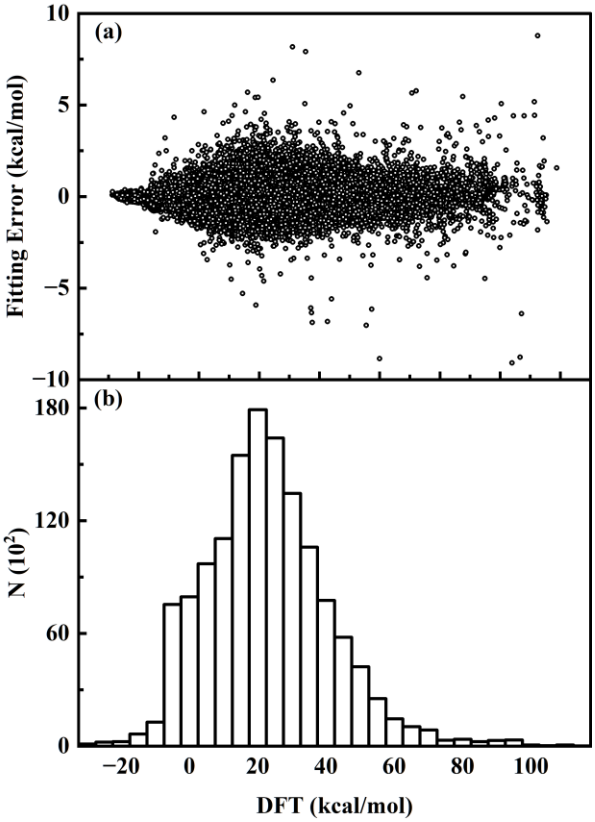

Figure 4. (a) Fitting error of PESL as a function of the DFT energy relative to the reactant asymptote. **(b)** Distribution of the DFT dataset.

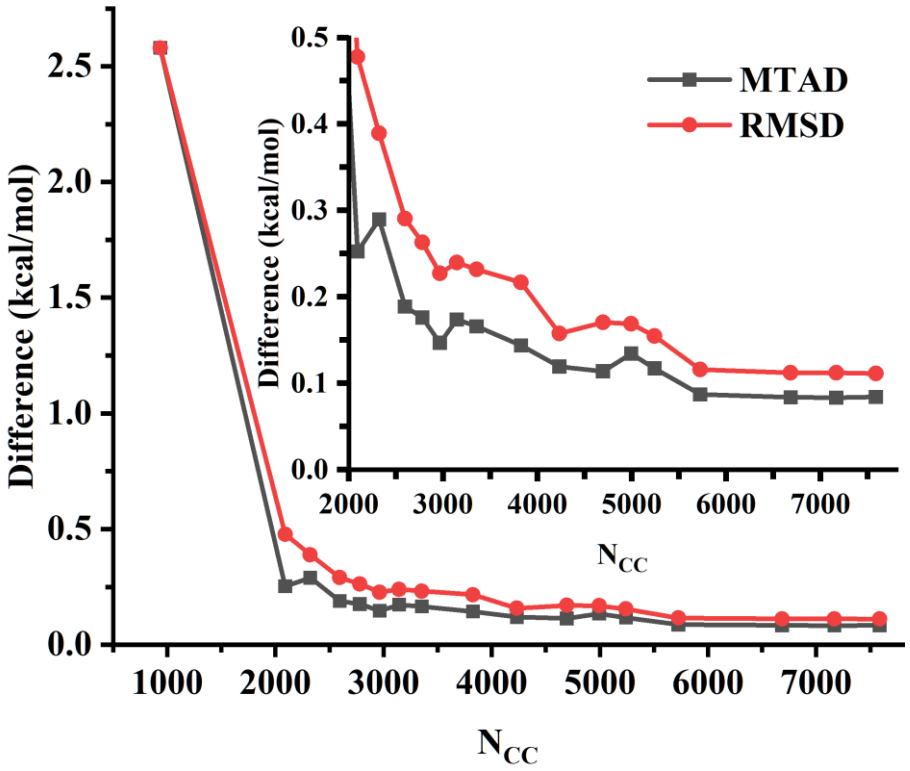

Figure 5. Dependence of MTAD and RMSD for the correction PES on the number of points (N_{CC}) calculated by the high-level method, namely, UCCSD(T)-F12a/AVTZ.

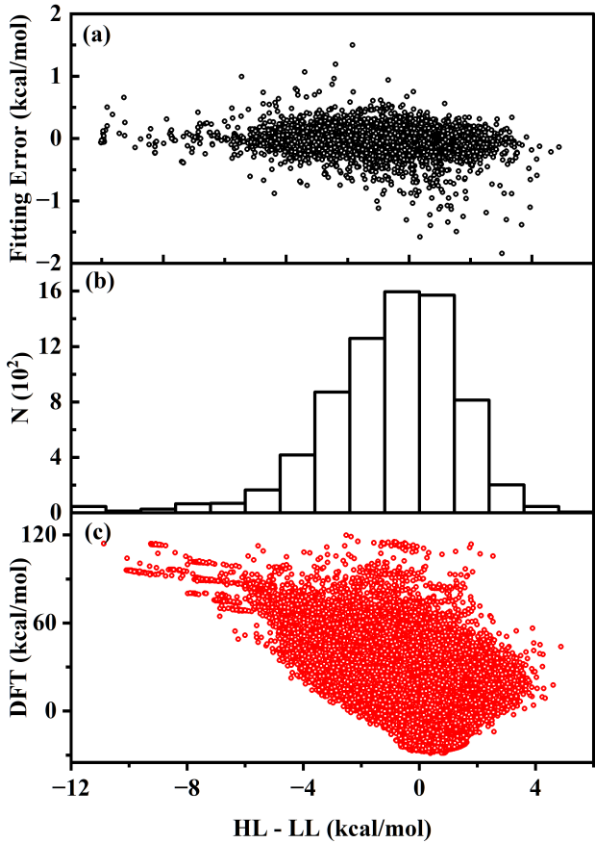

Figure 6. (a) Fitting error (E_{fit}-E_{target} in kcal/mol) of ΔV_{HL-LL} as a function of the target energy, the energy difference (HL – LL). **(b)** Distribution of the CC points for $\triangle V_{HL-LL}$. The bin size is 1 kcal mol^{-1}. **(c)** DFT energy vs. Energy difference (HL – LL) for the CC dataset.

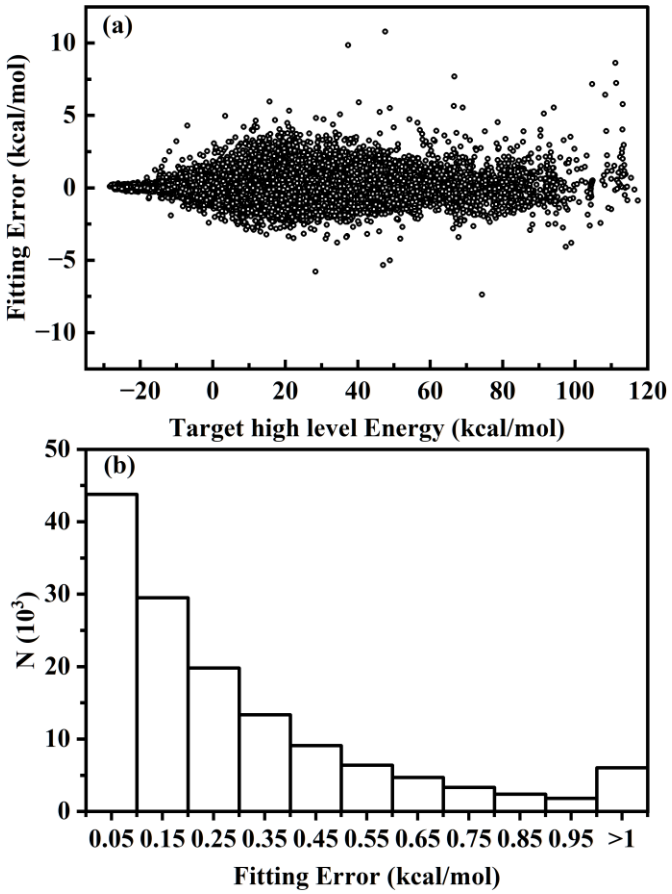

Figure 7. (a) Fitting error of PESH as a function of the target high level energy (UCCSD(T)-F12a/AVTZ) relative to the reactant asymptote. **(b)** Distribution of absolute fitting error of PESH.

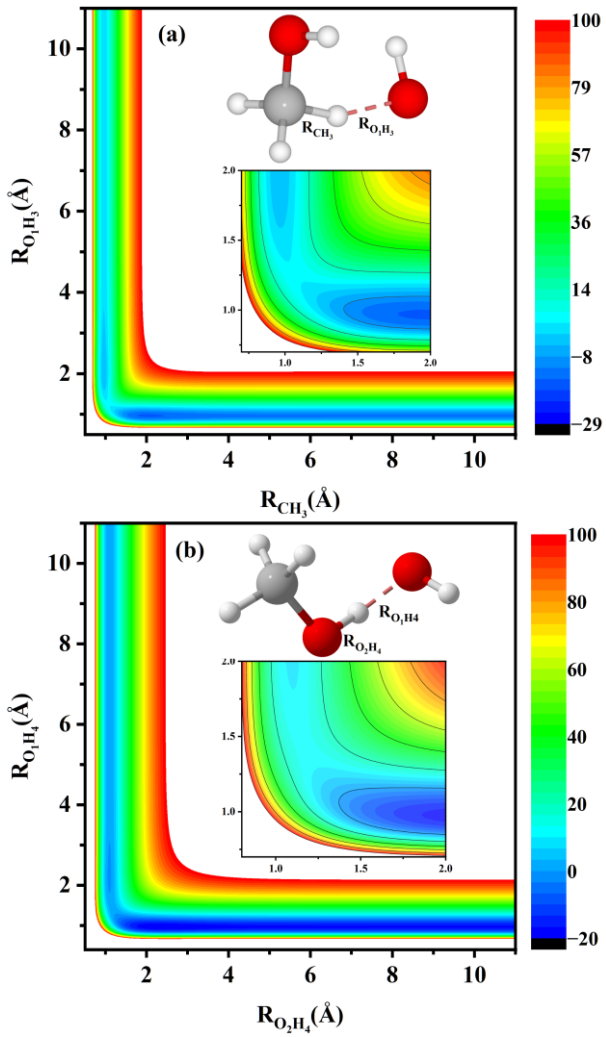

Figure 8. (a) Contour plot for R1 on PESH as functions of two reactive bonds R_{CH3} and R_{O1H3} with other coordinates fixed at TS1. **(b)** Contour plot for R2 on PESH as functions of two reactive bonds R_{O2H4} and R_{O1H4} with other coordinates fixed at TS2.

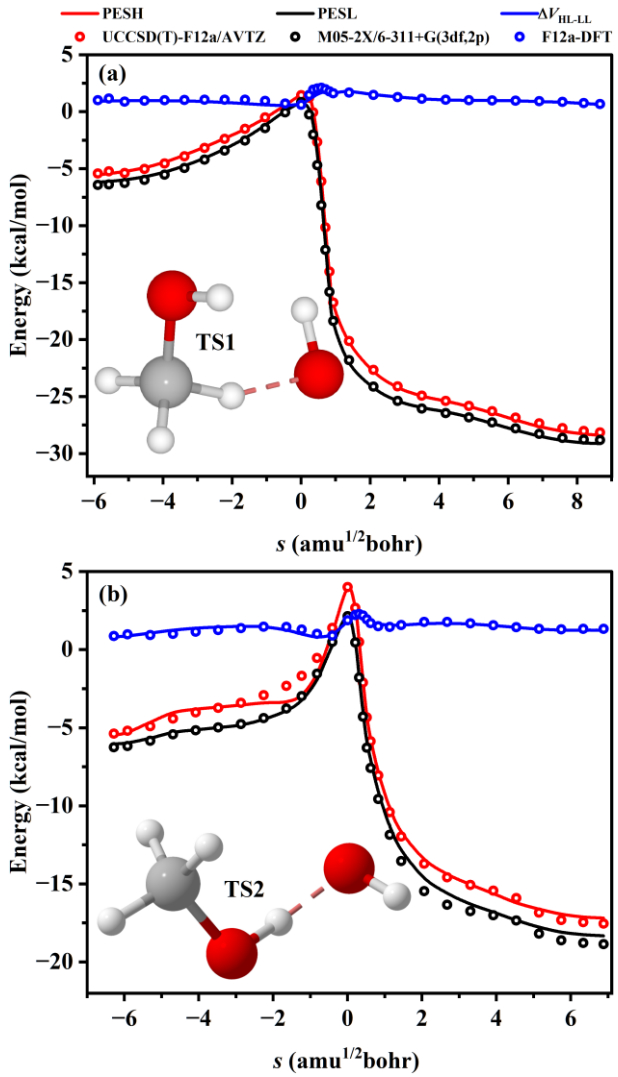

Figure 9. (a) Potentials along MEPs from RC to PC1 on PESH and PESL, and determined directly by HL and LL calculations. The energy differences between UCCSD(T)-F12a/AVTZ and DFT and the corresponding energies on $\triangle V_{\text{HL-LL}}$ are also included for comparison. **(b)** Similar to **(a)** but for the MEP from RC to PC2.

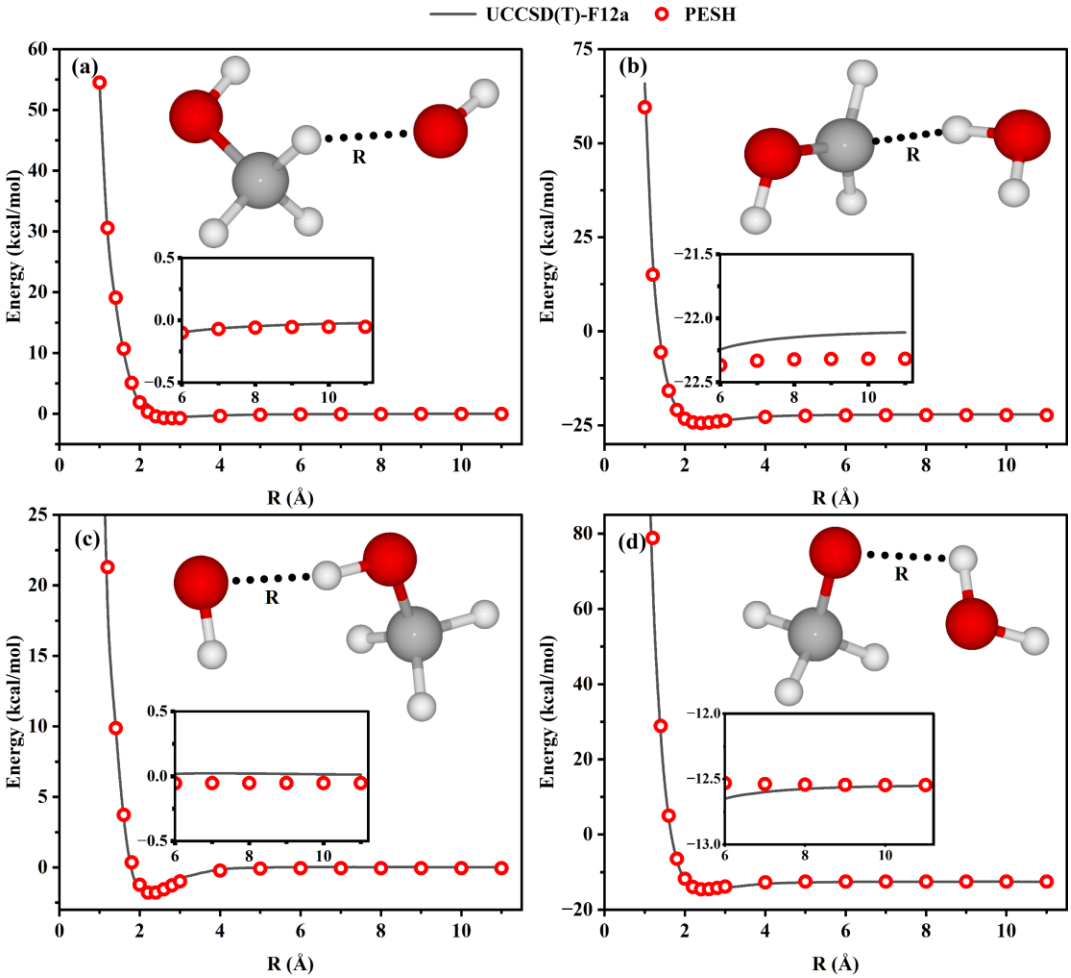

Figure 10. Several 1-dimensional (1D) cuts for the interaction energy between OH and CH_3OH or between CH_2OH and H_2O, or between CH_3O and H_2O at different configurations with other coordinates fixed at the equilibrium of the monomer.

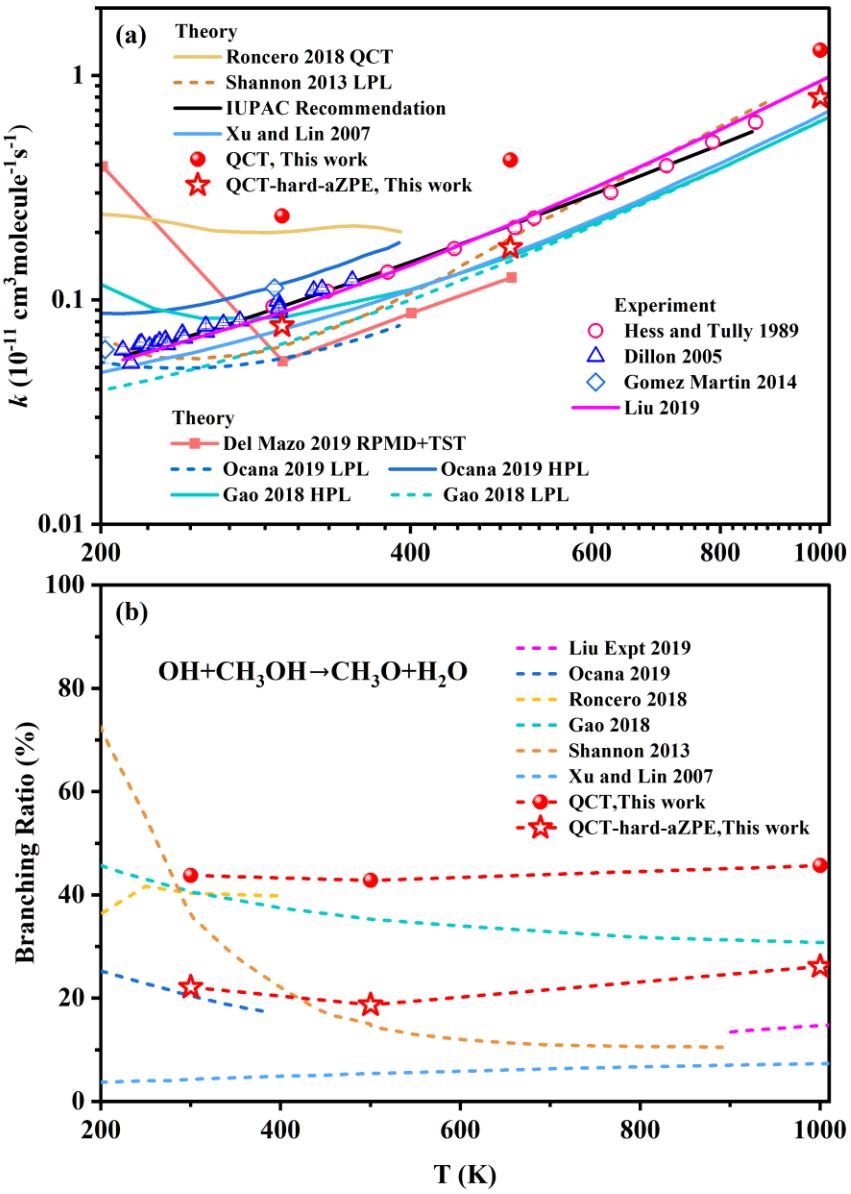

Figure 11. (a) Comparison of the rate coefficients of the title reaction from most available experimental and theoretical values with present work between 200-1000 K. **(b)** Branching ratios for reaction channel of R2 from theories in the LPL regime and experiments between 200-1000 K.